Acta Materialia 135 (2017) 314–329

Contents lists available at ScienceDirect

Acta Materialia

journal homepage: www.elsevier.com/locate/actamat

Full length article

On the microtwinning mechanism in a single crystal superalloy

D. Barba [a], E. Alabort [a], S. Pedrazzini [b], D.M. Collins [b], A.J. Wilkinson [b], P.A.J. Bagot [b], M.P. Moody [b], C. Atkinson [c], A. Jérusalem [a], R.C. Reed [a, b, *]

[a] Department of Engineering Science, University of Oxford, Parks Road, Oxford, OX1 3PJ, United Kingdom
[b] Department of Materials Science, University of Oxford, Parks Road, Oxford, OX1 3PH, United Kingdom
[c] Department of Mathematics, Imperial College, London, SW7 2BZ, United Kingdom

ARTICLE INFO

Article history:
Received 3 April 2017
Accepted 31 May 2017
Available online 5 June 2017

Keywords:
Microtwinning
Superalloy
Diffusion
Creep
Segregation

ABSTRACT

The contribution of a microtwinning mechanism to the creep deformation behaviour of single crystal superalloy MD2 is studied. Microtwinning is prevalent for uniaxial loading along ⟨011⟩ at 800 °C for the stress range 625 to 675 MPa and 825 °C for 625 MPa. Using quantitative stereology, the twin fraction and twin thickness are estimated; this allows the accumulated creep strain to be recovered, in turn supporting the role of the microtwinning mode in conferring deformation. Atom probe tomography confirms the segregation of Cr and Co at the twin/parent interface, consistent with the lowering of the stacking fault energy needed to support twin lengthening and thickening. A model for diffusion-controlled growth of twins is proposed and it is used to recover the measured creep strain rate. The work provides the basis for a thermo-mechanical constitutive model of deformation consistent with the microtwinning mechanism.

© 2017 Acta Materialia Inc. Published by Elsevier Ltd. This is an open access article under the CC BY-NC-ND license (http://creativecommons.org/licenses/by-nc-nd/4.0/).

1. Introduction

Resistance to plasticity is a significant advantage of the Ni-based superalloys, particularly when in single crystal form [1,2]. But a distinction must be made between the time-dependent mode of deformation – so-called creep deformation – prevalent at high temperatures and/or low strain rates [3–5] and the time-independent – commonly athermal – behaviour [6,7] which dominates at ambient conditions – see Fig. 1. Clearly, since many technological applications require the analysis of deformation behaviour, it is important to know which of the two modes is more likely. This challenge – which has still to be overcome – becomes even more daunting under the loading conditions at which the athermal and creep responses are approximately equal [8–13]. For the single crystal superalloys the situation is made more acute by the finding that a time-dependent viscous deformation mode involving the propagation of microtwins [9,10,14–17] can occur at this cross-over point – see Fig. 1.

The microtwinning mechanism was first postulated by Kear et al. [18] in the 1970s as a viable mode of deformation in the superalloys. Since then, several authors have reported the formation of microtwins in both single- and polycrystalline superalloys at many different temperatures and stresses – see Fig. 2. It seems reasonable to believe that the kinetics of the microtwinning mechanism depend strongly upon alloy chemistry but also on microstructural features such as precipitate size or alloy type: e.g., single- or polycrystalline systems. Originally, Kear et al. [18] assumed that the formation of microtwins occurs as a consequence of the formation of isolated superlattice intrinsic stacking faults (SISFs) in γ' which coalesce at high values of strain. This was believed to be driven by the annihilation of dislocation pile-ups of opposite sign. Later, Knowles and Chen [19] proposed instead an autonomous system of dislocations creating a twin band behind them. A somewhat different mechanism was proposed first by Kolbe et al. [15] and then later adapted by Kovarik et al. [10], in which the need for localised atomic diffusion was emphasised as indicated in Fig. 3. In this model, the set of proposed dislocations leads to a high-energy faulted structure (the so-called complex stacking fault, CSF) which, after a four-step atomic reordering process, regresses to a perfect crystal structure with an effective rotation of 60° with respect to the parent crystal. Unfortunately, even though these models explain succesfully the atomic deformation path leading to the final rotated configuration, they offer no satisfactory explanation for how the dislocations overcome the initial energy barrier imposed by the CSF which is very high, of the

* Corresponding author. Department of Engineering Science, University of Oxford, Parks Road, Oxford, OX1 3PJ, United Kingdom.
E-mail address: roger.reed@eng.ox.ac.uk (R.C. Reed).

http://dx.doi.org/10.1016/j.actamat.2017.05.072
1359-6454/© 2017 Acta Materialia Inc. Published by Elsevier Ltd. This is an open access article under the CC BY-NC-ND license (http://creativecommons.org/licenses/by-nc-nd/4.0/).

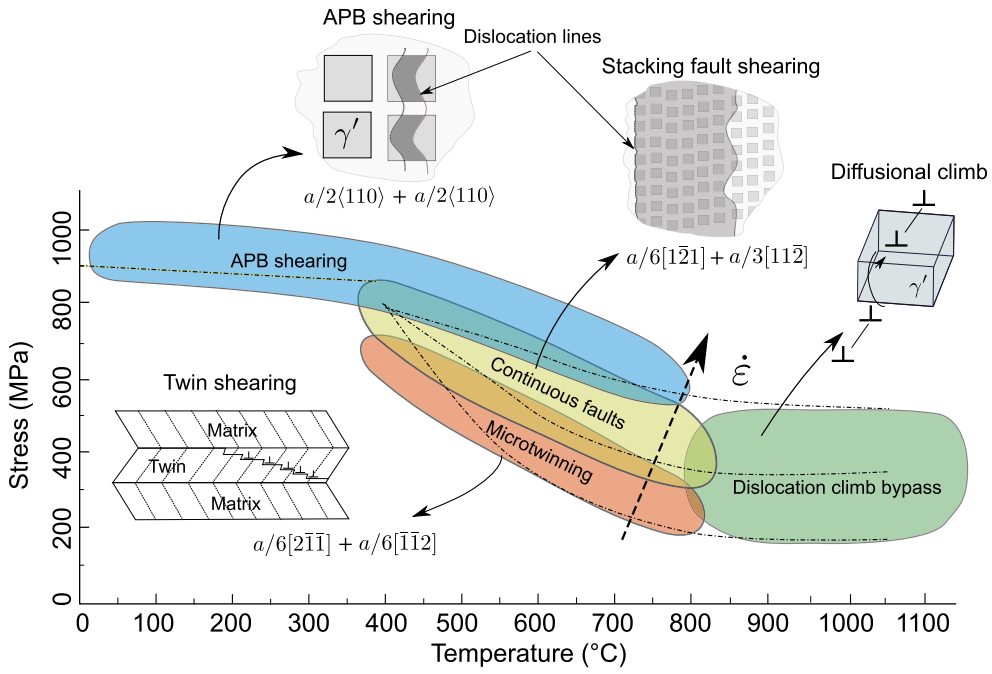


Fig. 1. Deformation map for a single crystal superalloy illustrating the dependence on stress, temperature and strain rate. Adapted from Smith et al. [21].

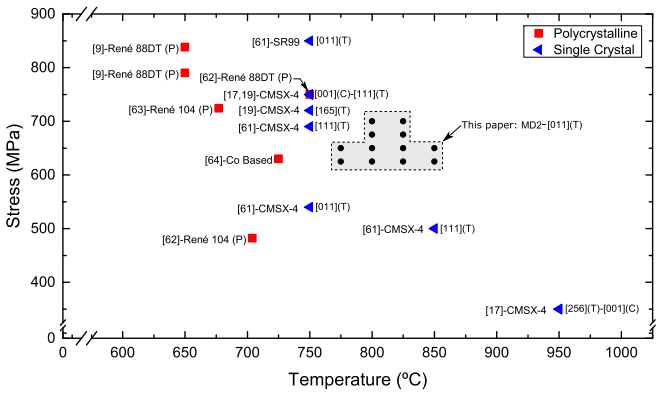


Fig. 2. Microtwinning conditions observed in the literature [9,17,19,61–64].

order of 300 mJ/m^2. The chemical fluctuations reported recently around faulted structures after mid-temperature deformation (600 – 800 °C) may address this conundrum [10,20–22]. In a series of Co-based superalloys, Titus et al. [23] reported partitioning of heavy elements such as Co, Cr, W and Ta to stacking faults (SFs), of both extrinsic (SESF) and intrinsic (SISF) type. Furthermore, Smith et al. [24] observed the segregation of Co, Nb, Ti and Ta along the SESFs and the formation of a high-density Co/Cr atmospheres enclosing the fault tips. Atomistic simulations indicate that the segregation of these elements lowers the energy of the SF [23–25], thus in principle stimulating the growth of the fault. Recently, Barba et al. [20] and Smith et al. [21,25] have extended the segregation studies to microtwins, finding again Co and Cr segregation at the microtwins within the γ' phase.

There is a clear similarity to classical deformation twinning [26], since there is a well-defined crystallography involving a twin plane and shear. On the other hand, some characteristics of a diffusional phase transition are displayed: for instance, there is a need for diffusion in the vicinity of the twin/matrix interface [9,10,15,27,28] and enrichment with regard to solute atoms in substitutional lattice sites [10,20,21], often at the twin/matrix interfaces [10]. Thus in some ways one should consider microtwins to form by a coupled diffusional/displacive mechanism of the type proposed for other alloy systems [29–34].

At the present time, multiple qualitative aspects of microtwinning have been identified, but many questions concerning such microtwinning effect remain unanswered. For instance, what are the rate-controlling processes needed for twin lengthening, and how can these be described mathematically? How are these related to the phenomena needed for twin thickening? Can the dependence on alloy composition be explained? Moreover, why does the diffusive shuffle appear to be best accommodated not by the nickel solvent but instead by other substitutional alloying elements? What is the mechanism by which the thickening of the microtwins is retarded? And most importantly, can the deformation on the microscale due to the microtwins explain the macroscopically observed time-dependent response?

The present paper – which is motivated by the above – is organised as follows. First, experimental measurements are made on a prototype Ni-based superalloy to enable typical creep rates but more importantly twin dimensions to be established. The chemical composition, microstructure and loading direction are fixed, thus allowing for the influence of temperature and stress to be studied quantitatively. Measurements of the segregation field around the twins are also made. Second, a detailed model is presented for the propagation of microtwins in these materials, which respects the underlying crystallography but also the diffusion and concentration fields which are observed experimentally. From this emerge estimations of the twin lengthening/thickening kinetics. Finally, we demonstrate that the proposed model allows the macroscopically-observed creep rates to be recovered.

2. Experimental methods

2.1. Material

The prototype single crystal Ni-based superalloy MD2 was used

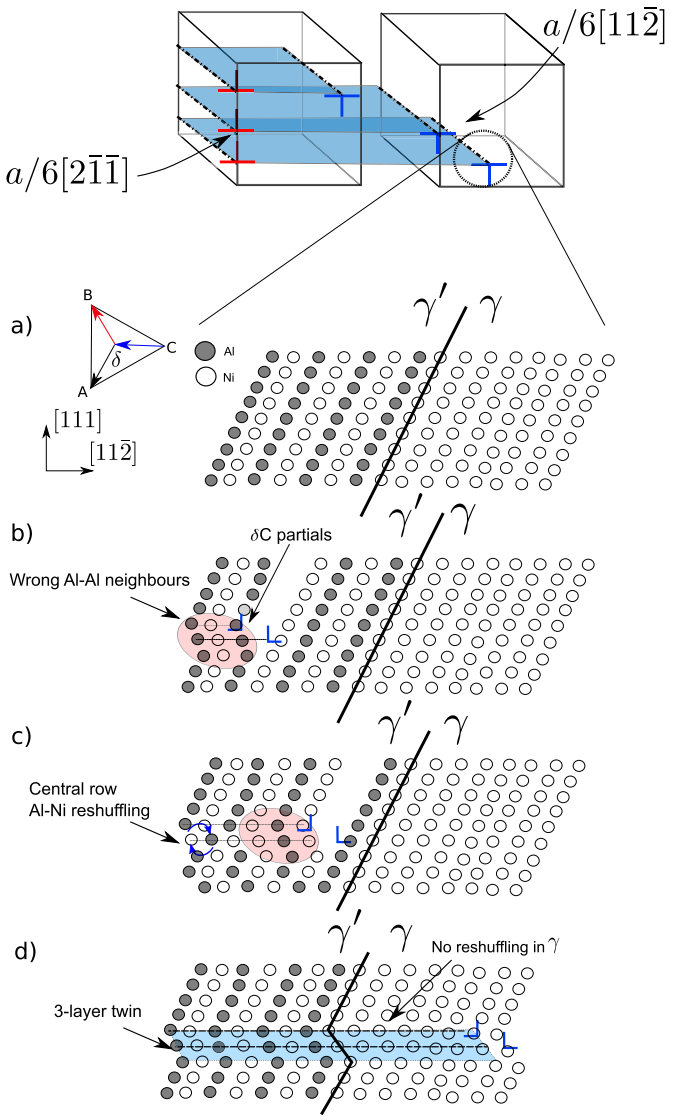


Fig. 3. Microtwin formation theory proposed initially by Kolbe [15] and later extended by Kovarik et al. [10]: a) initial γ/γ' crystal structure; b) a pair of δC partials on consecutive planes creates a two-layer CSF within the γ' precipitate; c) this CSF is transformed into a twinned structure by short range atomic reordering at the nucleus of the fault enabling the consequent shearing of the partials; d) a three layer microtwin is finally formed by the passage of the partials without the need of local reordering at the γ phase.

in the present study. Its nominal chemical composition is given in Table 1. Single crystal castings were produced in rod form using standard investment casting routes and solution treated for 8 h at 1275 °C, then aged following a two-step process: 6 h at 1080 °C and 16 h at 870 °C to yield a uniform distribution of γ' recipitates.

2.2. Creep testing

Miniaturised specimens of $1.6 \times 1\ mm^2$ cross-section were machined along the longitudinal direction of ⟨011⟩-oriented cast bars by wire-guided electro-discharge machining (EDM). Initial electron-backscattered diffraction (EBSD) analysis confirmed a maximum deviation of less than 4° from the ⟨011⟩ direction. Two twin systems, i.e., $(111)\text{-}\frac{1}{6}\left[\bar{2}11\right]$ and $\left(\bar{1}11\right)\text{-}\frac{1}{6}[211]$, are expected to activate during tensile deformation due to their large Schmid factors (0.47). Specimens were mechanically ground using 1200 grit SiC paper prior to testing to ensure a uniform and consistent surface finish. The testing temperature was controlled by a K-type thermocouple centrally welded onto the specimen. Digital image correlation (DIC) was used to measure the strain within the central 3 mm of the specimen [35]. The applied load was held constant either until rupture or until a maximum test duration of 50 h, depending which condition is achieved first.

Guided by the previous reported conditions for microtwinning (see Fig. 2), a series of creep tests were performed using an Instron electro-thermal mechanical testing (ETMT) machine at temperatures between 775 and 850 °C with applied engineering stresses of 625, 650, 675 and 700 MPa. Two tests were conducted for each test condition. The selected testing conditions for mapping microtwinning are summarised in Fig. 2.

Table 1
Chemical composition (wt.% and at.%) of Ni-based superalloy MD2.

	Ni	Al	Co	Cr	Hf	Mo	Ta	Si	Ti	W
wt. %	Bal.	5.0	5.1	8.0	0.1	2.1	6.0	0.1	1.3	8.1
at. %	Bal.	11.24	5.25	9.33	0.03	1.33	2.01	0.22	1.65	2.63

2.3. Microstructural characterisation

Metallographic examination of the samples was performed using a JEOL 6500F field emission gun scanning electron microscope (FEG-SEM) equipped with a TSL Digiview II EBSD detector. EBSD maps for geometrically necessary dislocation density calculations were obtained by locating each sample at a working distance of 15 mm, tilted 70° and oriented with the rolling direction parallel to the tensile axis, and therefore along the ⟨011⟩ cristallographic direction. EBSD diffraction patterns were acquired using a square grid with a 0.05 μm step size, a 30 kV accelerating voltage, 600 pA probe current and a 0.5 s acquisition time at the full 1000×1000 pixel resolution per pattern. A Matlab script [36] was then utilised to calculate lattice curvatures identified through the saved digitised diffraction pattern from each location within the square grid. Measured lattice rotations were subsequently used to calculate the spatially resolved geometrically necessary dislocation content [37]. Backscattered electron images (BEI) were acquired at 10 kV with a 300 pA probe size in order to exploit the channelling contrast created by the change in crystallographic orientation of the twins. Images in BEI mode of the twinned structures were used to perform a quantitative stereology assessment of the twin fraction and thickness. Equally spaced micrographs of $20 \times 20\ \mu m^2$ were taken to obtain a representative value of the twin fraction and thickness – starting from the fracture surface and moving along the tensile direction. The different twin fractions were statistically analysed in order to obtain a mean value for each testing condition within the central 3 mm of the sample. These results were used to map the twinned structure morphology as a function of the stress and the temperature. Additionally, EBSD low magnification maps of the previously BEI mode imaged regions were obtained using a Zeiss Evo LS1 W-filament SEM equipped with an Oxford Instruments EBSD detector. Finally, the fracture surfaces were characterised using an Alicona optical microscope.

Analysis of the chemical composition at the twin boundaries was performed at the atomic scale through atom probe tomography (APT). Samples for APT were prepared using a Zeiss NVision 40 focussed ion-beam microscope (FIB). Cantilevers $(25 \times 5 \times 5\ \mu m^3)$ were extracted from twinned regions in a sample which was tested at 800 °C and 650 MPa. A tungsten protective capping layer was applied to the cantilever surface before extraction, which was performed using a Kleindiek

micromanipulator. The cantilevers were then sectioned and mounted onto standard Cameca Si microtip coupons. Mounted samples were sharpened into tip sizes smaller than 100 nm in diameter. Finally, the tips were cleaned at 5 kV to remove the W capping layer and minimise gallium implantation damage. The tips were imaged repeatedly at 5 kV using the electron beam and InLens detector at every stage of the preparation in order to ensure the presence of a twin fault in the final needle. The samples were analysed using a Cameca LEAP 5000 XR instrument equipped with a UV laser, at 150 kHz pulse rate, 150 pJ pulse energy and a stage temperature of −223 °C. Reconstructions were performed using the Cameca IVAS 3.6.12 software.

3. Results

3.1. Identification of temperature/stress regime for microtwinning

Microtwinning has been proven to be active at 800 °C and 825 °C under stress conditions between 625 – 675 MPa and at 625 MPa, respectively. The creep results for temperatures of 775 °C, 800 °C, 825 °C and 850 °C are shown in Fig. 4. EBSD inverse pole figure maps of the deformed regions after testing are shown in Fig. 5. Under some conditions, band-shaped regions of a dissimilar orientation are identified; these extend through the entire sample width. The misorientation profile analysis identifies a 60° lattice misorientation about ⟨111⟩ between the deformation bands and the matrix. This is conclusive proof that microtwinning occurs. Moreover, the microtwin bands arrange in parallel bundles. This indicates that only one twin system is active during creep. The morphology of the microtwins depends significantly on the testing conditions. This dependency is intimately related to the microtwinning kinetics: both lengthening and thickening. Their kinetics are quantitatively analysed in the following section.

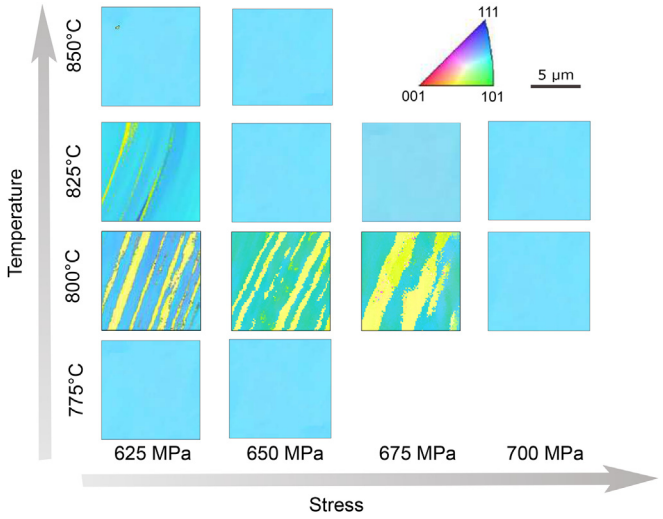


Fig. 5. EBSD analysis for MD2 specimens after creep tests at the conditions presented in Fig. 4.The change of orientation indicates the formation of microtwins.

The steady-state creep stage is now analysed, identifying the type of mechanisms taking place. The secondary creep rates are plotted in Fig. 6 differentiating between testing conditions where microtwinning mechanism is active (red) and conditions where no

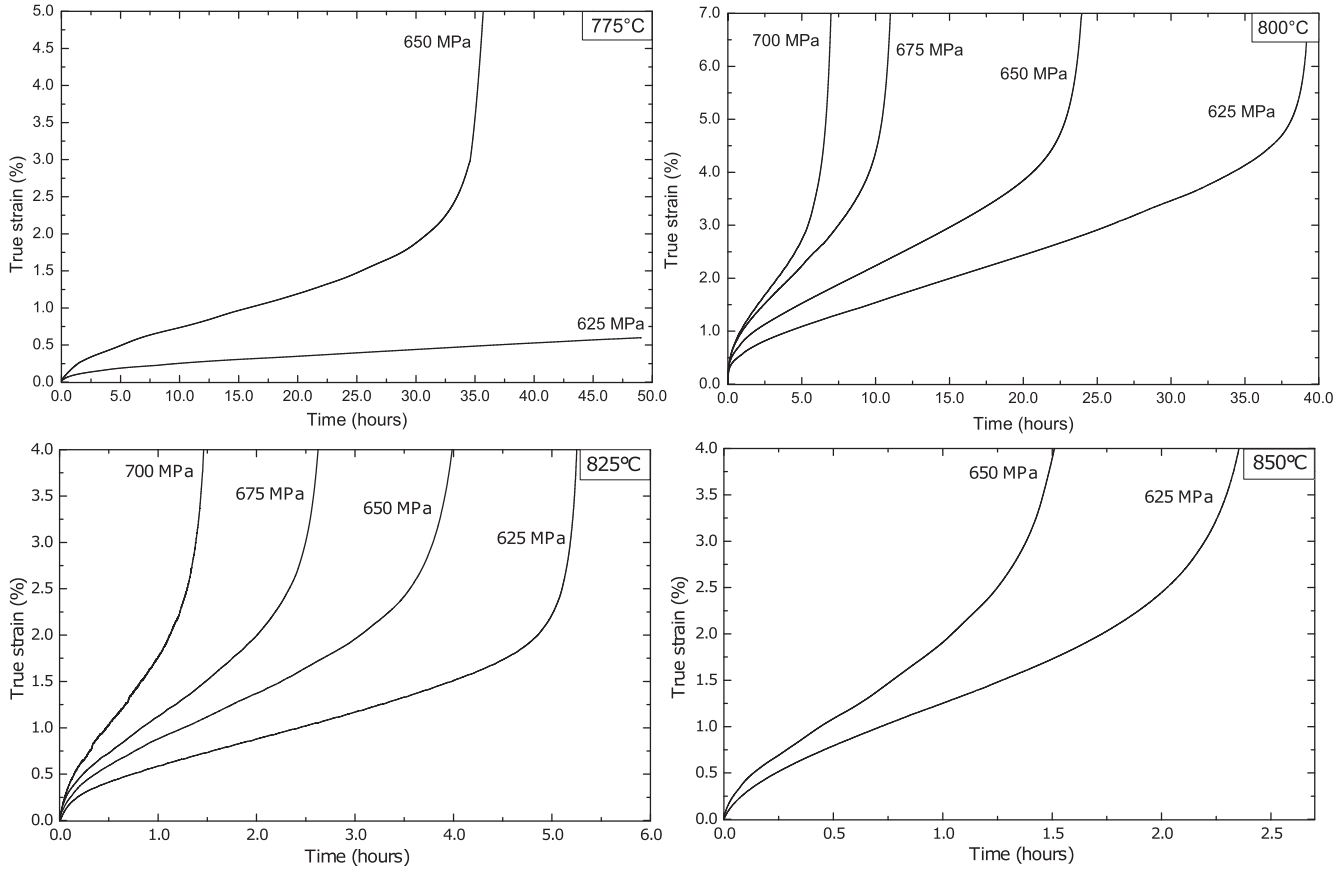


Fig. 4. Creep strain curves for single crystal MD2 at 800 °C, 825 °C and 850 °C and stresses between 625 MPa to 700 MPa.

microtwinning was observed (black). The activation volumes and the activation energies for both cases are indicated as a function of the temperature and the stress, respectively. No appreciable change of the apparent activation energies and activation volumes between twin and non-twin conditions is observed. The apparent activation energy values (400–480 kJ/mol) are in agreement with previous studies [38,39] for the same range of temperatures but substantially higher than the value of self-diffusion of nickel ($Q_{self} \approx 300$ kJ/mol) which suggests that other diffusive processes different than this one may be taking place. Similarly, the activation volume values (200–300 b^3, where $b = 1.4 \times 10^{-10}$ m is the Burger vector) are in agreement with previous studies [5] at similar temperatures.

3.2. Estimation of microtwin thickness and fraction, and stress/temperature dependence

The twin bands identified by EBSD analysis are composed of bundles of thinner microtwins which, due to EBSD spot size limitations, appear as a single entity in Fig. 5. To overcome this, high-resolution backscattered imaging is used to provide more accurate thickness and twin fraction (f_{twin}) measurements as indicated in Fig. 7a. Both twin fraction and thickness are found to increase with stress, see Fig. 7b–c. In contrast, the twins appear in less quantity and are thinner as the temperature increases.

The following is noted: (i) there is a critical stress for twin partial dislocation nucleation that probably represents the transition between dislocation climb or fully diffusional creep and the microtwin-stacking fault regime; (ii) as the stress increases, the

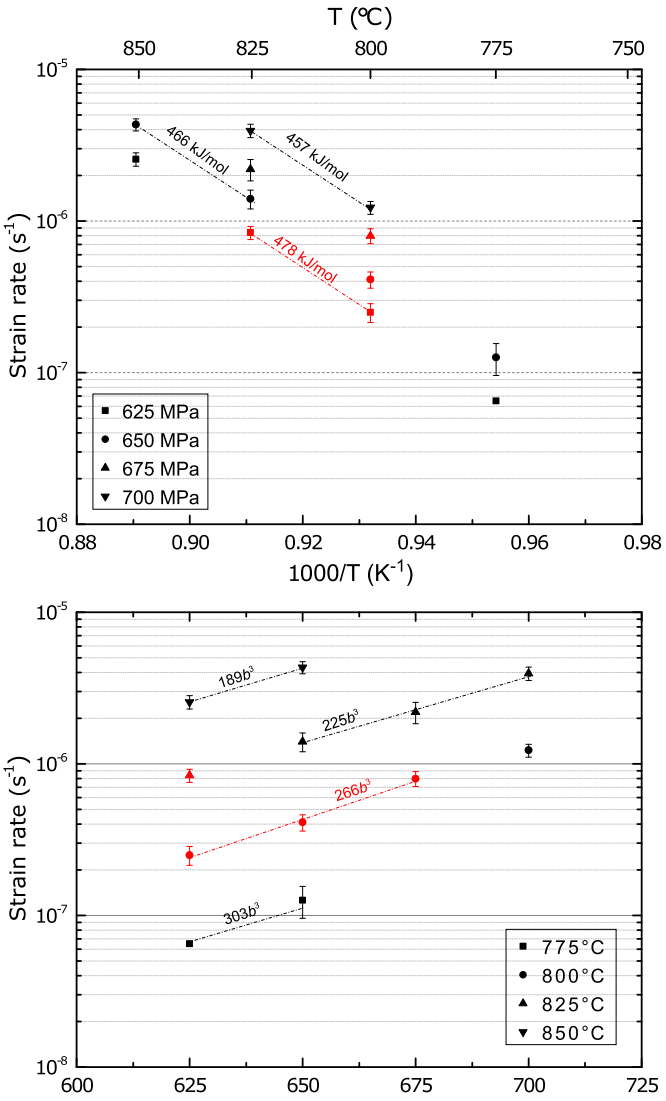


Fig. 6. Top: Activation energy analysis for MD2 single crystal. Red points represents microtwinning conditions. The activation energy values are indicated as the slope of the linear fit. Bottom: Activation volume analysis of the same material. The activation volume values are provided as the slope of the linear fit. (For interpretation of the references to colour in this figure legend, the reader is referred to the web version of this article.)

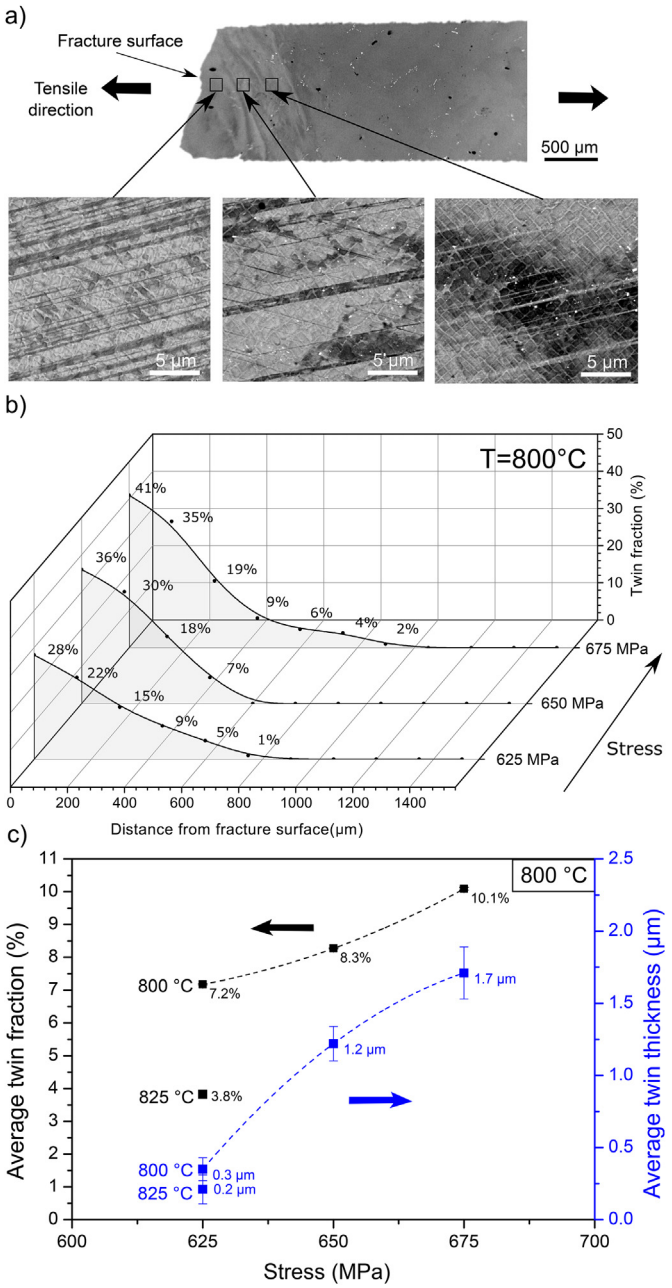


Fig. 7. a) Tested specimen at 800 °C and 650 MPa with detailed micrographs of the twin structures at 150 μm, 300 μm and 450 μm from the cracked surface; b) twin fraction measurements as a function of distance from the fracture surface along the tensile axis of the specimen for samples tested at 800 °C; c) averaged twin thickness and twin fractions within the central 3 mm of MD2 samples after creep deformation at different temperature and stress levels calculated from results in b).

nucleated partial dislocation population grows as a direct effect (625–675 MPa at 800 °C); (iii) when the stress reaches a critical threshold, dislocation anti-phase boundary (APB) shearing becomes favourable to the detriment of microtwin formation (700 MPa at 800 °C). The evolution of these three stages is consistent with the schematic deformation map proposed in Fig. 1.

3.3. Rationalisation of the contribution of the microtwinning mechanism on the overall creep strain

Microtwinning is responsible for the majority of the creep strain at 800 °C. The microscopic shear strain produced by microtwinning can be defined as:

$$\gamma_{twin} = s f_{twin} \quad (1)$$

where f_{twin} is the averaged twin fraction within the gauge length and s is the shear produced by a completely twinned crystal [26]. The average twin fraction f_{twin} within the central 3 mm of each sample is presented in Fig. 7c. The shear strain s is defined as $s = b/h$, where h is the spacing between the {111} shear planes. For the case of the highest Schmid factor $\frac{1}{6}[\bar{2}11]$ twin partial (0.47), $s = \frac{\sqrt{2}}{2}$. The macroscopic longitudinal twin creep strain ε_{twin} can be recovered from:

$$\varepsilon_{twin} = \sqrt{1 + \gamma_{twin}^2 \cos^2\phi + 2\gamma_{twin} \cos\phi \cos\lambda} \quad (2)$$

where ϕ and λ are the angles between the tensile axis and the normal to the twin plane and twin direction, respectively [40]. For the ⟨011⟩ case, $\phi = 35.3°$ and $\lambda = 54.7°$. This strain from microtwinning shearing is presented in Fig. 8.

In order to compare the contribution of the microtwinning shear to the overall creep strain, the primary + secondary and the primary + secondary + tertiary creep strains (for until rupture tests) are displayed. During the tertiary creep, the cross-section reduction caused by necking leads to a proportional increase of the stress in the tested sample. Because of the high sensitivity of microtwinning to testing conditions as indicated in Fig. 5, it seems reasonable to assume that the creep regime where microtwinning is active is constrained to the primary and secondary creep stages of the tests. With this in mind, microtwinning shearing accounts for the majority (73%–96%) of the total plastic strain, especially at higher stresses (700 MPa), both within the primary and the secondary creep stages. From these results, the confinement of the plastic strain to just one twin system is believed to be accommodated by slip and/or rotations outside the gauge length.

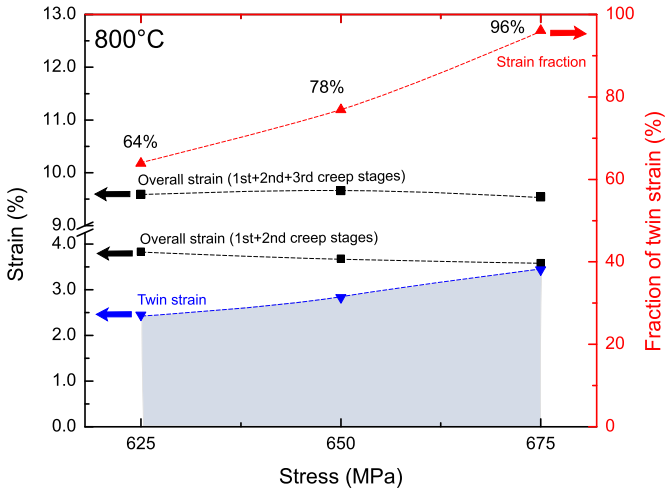


Fig. 8. Measured total creep strain and calculated twin strain, both before necking, after creep deformation at 800 °C. The indicated twin strain fraction is with respect to the primary + secondary creep strain.

3.4. Characterisation of twin boundary segregation

Local enrichment of Cr and Co has been found at the twin-matrix interfaces within the γ' phase. The APT samples were extracted from post-mortem specimens tested at 650 MPa and 800 °C as indicated in Fig. 9a. The locations of the twin boundaries within the needles were identified through apparent localised density variations visible in the form of three parallel planar features as shown in Fig. 9b. These regions have been shown to be linked with fault interfaces in the work of Barba et al. [20]. Two of the analysed APT samples contain microtwins. The three-dimensional atom maps of one of these needles are shown in Fig. 9b. The one-dimensional concentration profiles along a cylindrical region containing the three microtwins in the needle are detailed in Fig. 9c confirming the local enrichment of Cr and Co at the boundaries. The peak values for MD2 alloy are consistent with the findings of Smith et al. [24] for ME3 and Viswanthan et al. [41] for CMSX-4. These, in conjunction with the compositions presented in Barba et al. [20], are used to calculate the diffusion field around the microtwins in the following section. Nevertheless, the implications of these findings on the microtwinning kinetics need further rationalisation.

4. Discussion

In this section, modelling is used to rationalise the experimental observations. First, the underlying mechanisms – diffusion and shearing – are coupled using a physically-faithful approach. Then, the predictions are compared with the experimentally observed macroscopic behaviour. The procedure is as follows: (i) the twin lengthening kinetics are modelled and the velocity of the microtwin dislocations are estimated; (ii) a homogenisation framework is developed to obtain the macroscopic strain rate from the calculated velocity. Second, a microtwin nucleation theory is proposed. This leads to a nucleation map dependent on the crystal orientation and stress state where the influence of the fault energy is considered. Finally, the implications and ramifications of this work are discussed.

4.1. Kinetics of microtwin formation

The observations of segregation to faulted regions are consistent with those reported for other superalloys [20,22–24,41]. Although the elements which segregate may differ from one alloy to another, Co and Cr are commonly observed at the faults [20,22,24,41]. These exhibit pronounced concentration increments of ≈ 0.5–1.0.at.% at the fault line or, in the case of microtwins, at the fault boundaries as shown in Fig. 9. Moreover, one should consider SESFs as microtwin embryos that, given the appropriate stress and temperature conditions, thicken to form full twins. Therefore, in either microtwinning or SESF formation, it would be reasonable to assume that similar kinetics are applicable [10,15,24,41].

Previously, Smith et al. [24] proposed a dislocation decorrelation system $2 \times \frac{1}{6}[11\bar{2}]$ consistent with the high Schmid factor criterion for compression tests along the ⟨001⟩ direction. In this case, it can be observed that the active dislocation system involves $\frac{1}{6}[\bar{2}11]$ type dislocations which exhibit the highest Schmid factor (0.47) for tensile ⟨011⟩ but that this model is applicable to any of the other

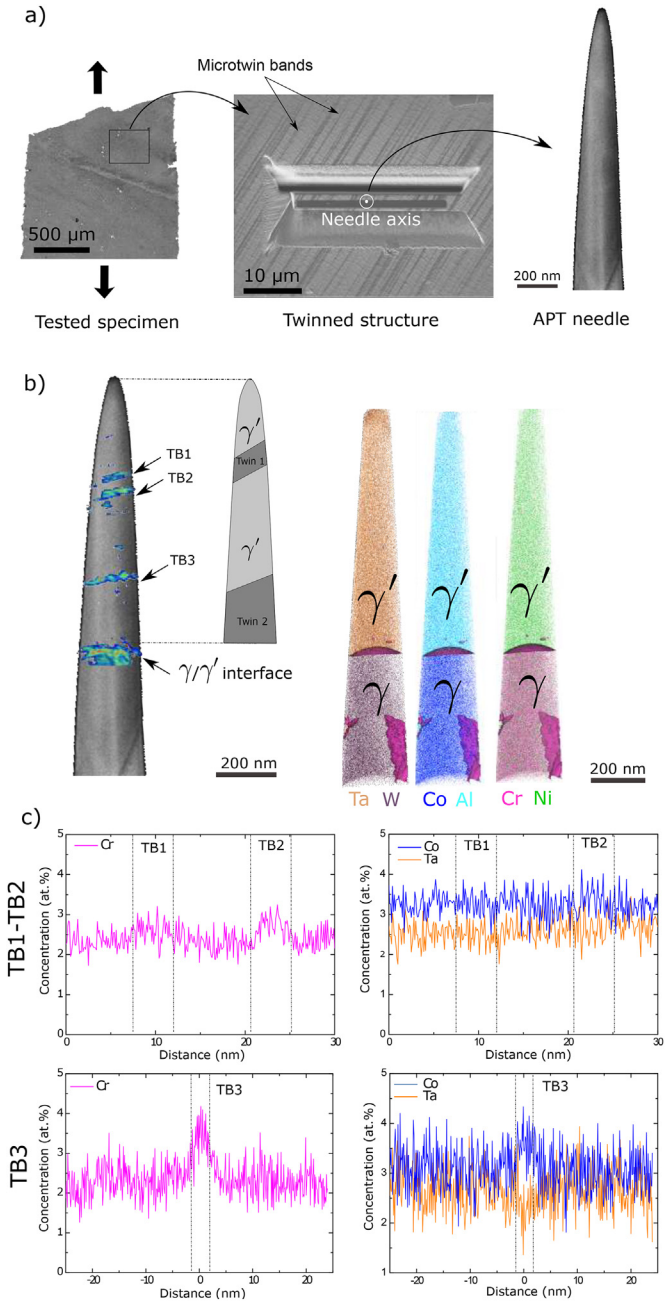


Fig. 9. a) Detail of the APT needle preparation process from a tested specimen at 800 °C and 650 MPa; b) higher atomic density planar features identifying the position of three fault interfaces within the γ' phase and atom maps with γ-γ' phase transitions; c) 1D concentration profile across the regions identified as twin boundaries showing segregation of Cr and Co at the microtwin-matrix boundaries in the γ' phase.

twin partials. The overall microtwin growth and thickening mechanism used here for the ⟨011⟩ tensile case builds on the work of Barba et al. [20]. First, a pair of complete dislocations is constrained to the γ/γ' interface as the applied creep stress is insufficient to overcome the high energy APB created. This dislocation system evolves to a lower energy structure of partial dislocations:

$$\begin{cases} \frac{1}{2}\left[\bar{1}10\right] \rightarrow \frac{1}{6}\left[\bar{1}2\bar{1}\right] + \frac{1}{6}\left[\bar{2}11\right] \\ \frac{1}{2}\left[\bar{1}01\right] \rightarrow \frac{1}{6}\left[\bar{1}\bar{1}2\right] + \frac{1}{6}\left[\bar{2}11\right] \end{cases} \quad (3)$$

leading to partials of highest Schmid factor for tensile ⟨011⟩ which are able to shear the precipitate. This forms a two-layer CSF similar to the ones described first by Kolbe [15] and later confirmed by Smith et al. [24]. Partitioning of Co and Cr to this fault lowers the high energy penalty by transforming it into a lower energy stacking fault. This process will leave enough time for the necessary atomic reshuffling to occur in order to annihilate the wrong neighbours structure, thus enabling the lengthening of the twin. Shearing of the same type of partial dislocations on consecutive planes will produce the thickening of the twin, possibly also dependent on a surface energy term. This process differs from the theory first introduced by Kolbe [15], for which no long range diffusion was assumed necessary. In order to model the twin growth kinetics, one may assume that the two diffusion processes are simultaneously controlling the shearing of the partials: (i) the partitioning of Co and Cr into the body of the fault, and (ii) the short range reordering events behind the leading partials.

4.2. A model for microtwin formation

The mathematical procedure developed by Atkinson [42] is used here. It is assumed that growth is produced by the lateral movement of ledges. There are three different scenarios during twin growth that need to be considered and they are detailed in Appendix A. (i) Initially, the fault starts as a single thin plate of height h_t (equal to two atomic planes) growing within the matrix (as indicated in Fig. A1-scenario 1). Its lengthening is supported by long range diffusion of Co/Cr from the surrounding matrix. This scenario represents the twin embryo or SESF. (ii) Second, as the material continues deforming, the initial thin plate thickens by means of adjacent growing ledges as illustrated in Fig. A1-scenario 2. At this stage, the twin is still thin enough to assume that the growth of the adjacent ledges is still supported by significant long-range diffusion from the matrix as the mass available of Co/Cr for diffusion within the twin is still insufficient. As the twin thickens, the core of the twin depletes itself from solute, thus recovering the matrix composition and confining the segregation at the twin boundaries, where the atomic structure is still faulted. The new growing ledge can now be supported to some extent by the enriched ledges ahead. A mathematical study of the three different stages of the growth process is presented in Appendix A with special attention to the estimation of the velocities for each case.

Diffusion consistent with Fick's law is assumed. Mass conservation is imposed at the interface, leading to the so-called Stefan condition [42]:

$$v_t = D_{\text{eff}} \left.\frac{\partial c}{\partial X}\right|_{\text{step}} (c_t - c_p)^{-1} \quad (4)$$

where v_t is the twin step velocity, X is the absolute coordinate along the twin length, $D_{\text{eff}} = \frac{D_{Co}c_{Co} + D_{Cr}c_{Cr}}{c_{Co} + c_{Cr}}$ is the effective diffusivity of Co and Cr in the γ' parent phase and c_t and c_p are the effective Co + Cr concentrations ($c = c_{Cr} + c_{Co}$) in the twin phase and in the parent phase at the twin step, respectively, see Fig. 10a.

In addition to the diffusion problem around the step interface, there is also a short range atomic reordering at the interface which is necessary for the twin tip to advance and limits the interface mobility. The mobility of the interface μ_o is approximated using the thermally-activated dislocation theory [43,44] in which the probability of a dislocation advancing along the glide direction is associated with the free energy change of the event ΔG, in this case with the atomic reshuffling. This energy change $\Delta G = \Delta G_0 + \tau V$ includes the work done by the external shear stress τ against the zero-stress energy barrier of the reshuffling processes ΔG_0, where

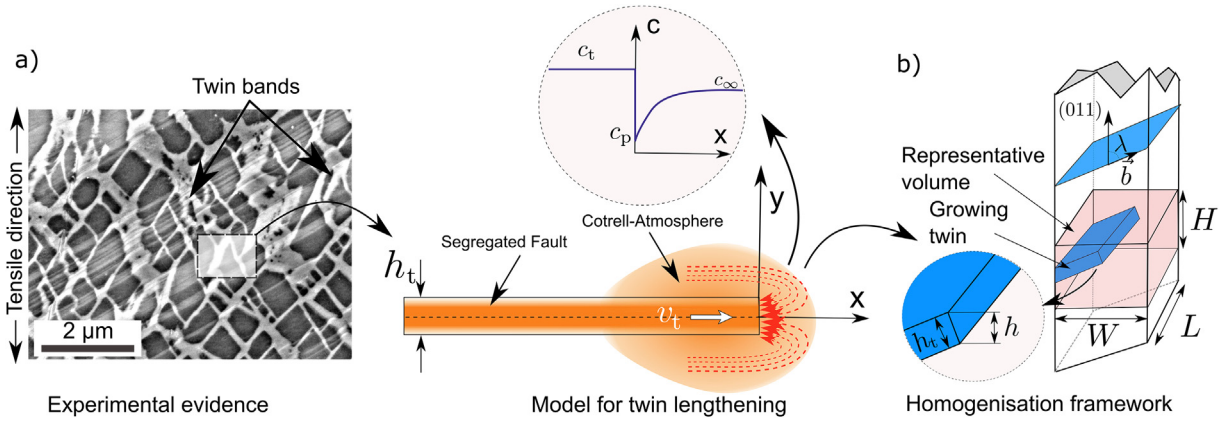


Fig. 10. a) Experimental evidence of microtwin bands; b) detailed diagram of the twin lengthening mathematical problem; c) geometrical diagram of the twin glide plane and the representative volume used in the homogenisation calculations.

$V = -\left(\frac{\partial \Delta G}{\partial \tau}\right)_T$ is the activation volume of the deformation mechanism. The energy barrier ΔG_0 associated with these reordering events has been studied in detail by Kovarik et al. [10] and is used here. The interface mobility can then be approximated as:

$$\mu_o = b\,\nu \exp\{-(\Delta G_0 - \tau\, V)/kT\} \tag{5}$$

where ν is the Debye frequency vibration of a reshuffled Ni atom [10], k is the Boltzmann constant and T is the absolute temperature. The effect of the interface mobility is included by adding an extra boundary condition ($v_t = \mu_0(c_p - c_e)$, where c_e is the Co + Cr equilibrium concentration in the matrix at the twin/matrix-interface). Further details of the mathematical treatment of the problem are provided in Appendix A.

The physical parameters (c_∞, c_e, c_t, D_{eff}, h_t, ΔG_0 and V) involved in the problem need to be estimated based on experimental measurements and thermodynamic estimates. The Co and Cr concentrations in the γ' at infinity (c_∞) are extracted using the averaged APT concentrations in the γ' far field from the twin. The compositions at the twin ledge interface (c_t) are calculated by averaging the integrated concentration between mid-points of the concentration peaks in the APT analysis. The concentration peaks from all the interfaces analysed here and in the previous work of Barba et al. [20] are considered. The γ' equilibrium composition (c_e) and the chemical diffusivities of Co and Cr (D_{Co} and D_{Cr}) are obtained using Thermo-Calc software (database TTNI8) and DICTRA (database MOBNI3) for equilibrium phase calculations and kinetics, respectively [45,46]. The activation volume V is derived from the data in Fig. 6, taking into account the tests where microtwinning is active at 800 °C. The activation energy for the short range reordering (ΔG_0) was determined as the addition of migration and vacancy formation energies following the work of Kovarik et al. [10]. Finally, the height of the twin step is set to twice the {111} spacing for γ' ($h_t = 2a_{\gamma'}/\sqrt{3}$, where the lattice parameter $a_{\gamma'}$ for MD2 is obtained from the measurements of Pyczak et al. [47] on the similar superalloy CMSX-4 using X-ray diffraction). The parameters used in the calculations of the diffusion field and dislocation velocities are given in Table 2.

The computed concentration field around a twin tip for the case of 800 °C and 650 MPa is illustrated in Fig. 11. The iso-concentration surfaces around the twin tip are ellipsoidal in shape. From these results, one deduces that the diffusion phenomena are not only constrained to a few atomic spacings (consistent with the necessary short-range reordering) but involve long range mass transport. From this concentration field, the twin ledge velocity is plotted in Fig. 12 as a function of the non-dimensional concentration and the non-dimensional interface mobility $q = \mu_0(c_t - c_e)(2D/h_t)^{-1}$. The specific case of 650 MPa and 800 °C ($q = 2 \times 10^5$) is highlighted. As a first approximation, the growth rate of the microtwin embryo and associated is of order of magnitude $v \sim D/h \sim 5 \times 10^{-9}$m·s^{-1}.

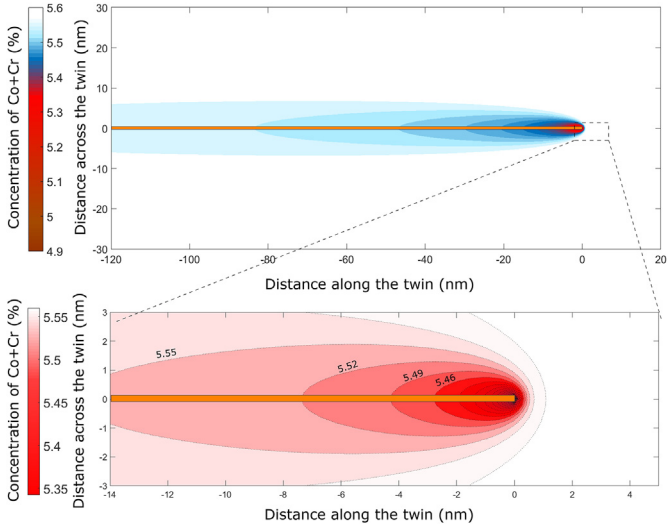


Fig. 11. Calculated Co + Cr concentration field for a leading twin tip growing at 800 °C (top) and detailed view with concentration stream lines of the concentration field indicating the shape of the diffusion field (bottom).

Table 2
Parameters used for calculating the twin dislocation velocities in MD2 Ni-based superalloy.

D_{Co} (m^2/s)	D_{Cr} (m^2/s)	D_{effe} (m^2/s)	c_∞(%)	c_t(%)	c_e(%)	h_t(m)	$V(b^3)$	ΔG_0 (eV)	ν
2.35×10^{-18}	1.77×10^{-18}	2.10×10^{-18}	5.62	6.35	4.99	$7/3\sqrt{3} \times 10^{-10}$	266.8	2.27	9.66×10^{13}

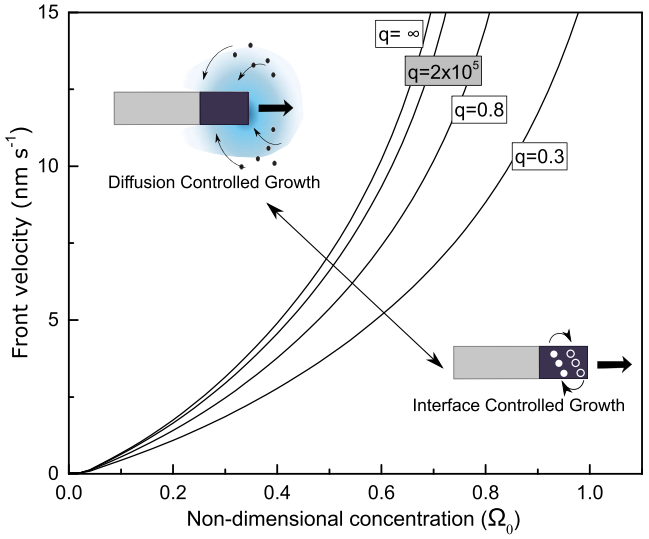


Fig. 12. Twin ledge growth velocity v_t against the non-dimensional concentration $\Omega_0 = (c_\infty - c_e)/(c_t - c_e)$ for different non-dimensional interfaces mobilities $q = \mu_0(c_t - c_e)(2D/h)^{-1}$.

4.3. Macroscopic homogenisation of the microtwin kinetics

To compare the lengthening rates computed with the experimental results, a homogenisation approach is taken. The shearing rate $\dot{\gamma}$ produced by the microtwinning mechanism is extracted from the growth rate of the twinned phase:

$$\dot{\gamma} = \dot{f}_{V-twin} s \tag{6}$$

where $\dot{f}_{V-twin}$ is the rate of change with time of the twinned volumetric fraction and s is the twin shear. By assuming the previously introduced ledge growth mechanism, the rate of change of volume fraction can be approximated as

$$\dot{f}_{V-twin} = \frac{n h_t l}{HLW} \bar{v}_t \tag{7}$$

where n is the number of twins ledges in the reference volume, h_t and l are the growing front dimensions of each twin ledge, $\bar{v}_t$ is the mean twin ledge velocity and H, L and W are the height, length and width of the reference volume as indicated in Fig. 10b, respectively. In this expression $nh_t(\cos\phi/H)$ is the average twin fraction calculated from the tested specimens where $h_t \cos\phi$ is the projection of the twin height on the tensile axis. In this approach we assume that the twins are growing homogeneously during the test until the final twinned structure is formed. The mean twin ledge velocity $\bar{v}_t$ corresponds to the averaged velocity across γ and γ', assuming instantaneous glide across the γ phase ($\bar{v}_t = v_t/f_{\gamma'}$, where $f_{\gamma'}$ is the γ' volume fraction). Taking this into account the overall creep rate can be rewritten as

$$\dot{\gamma} = \frac{f_{twin}(L+W)}{2LW f_{\gamma'} \cos\phi} v_t s \tag{8}$$

where the twin front width l is approximated by the averaged section chord $l = (L+W)/2$. Finally, for the case of single crystal, the Schmid angles (ϕ, λ) are used to relate the microscopic twinning shear strain rate $\dot{\gamma}_{twin}$, assuming a single activated twin system, to the tensile macroscopic strain rate $\dot{\varepsilon}$ following [40]:

$$\dot{\varepsilon} = \frac{d}{dt}\sqrt{1 + \gamma_{twin}^2 \cos^2\phi + 2\gamma_{twin}\cos\phi\cos\lambda} \tag{9}$$

All the quantities involved here are known from the experiments (f_{twin}, W, L) or are geometrical relations (ϕ, s). The twin fractions f_{twin} are obtained from image analysis on the micrographs cited in the previous subsection and presented in Fig. 7c. The width and thickness of the sample, W and L, are set to 1.6 mm and 1 mm, respectively. The full set of parameters used in this homogenisation framework is given in Table 3.

The calculated strain rates at 800 °C produced by microtwin shearing for the three stress levels where this mechanism is active are indicated in Fig. 13. The strain rates calculated are found to be a good approximation of the experimental ones without any free parameter calibration. Moreover, the model captures the observed strain rate dependence on the stress through the increase of the twin nucleation density (introduced by f_{twin}) and the assistance of the external stress on the interface reactions ($\Delta G = \Delta G_0 - \tau V$). The predicted values are always below the real strain rates; two factors may be relevant: (i) the twin volume growth rate may be larger than the proposed approximation due to several twin ledges advancing on the same shear plane; (ii) the shear rates calculated here are just the contribution of the microtwinning mechanism to the overall deformation – other mechanisms may be operative.

4.4. On the nucleation of microtwins

In this section, consideration is given to the factors determining microtwinning nucleation. In this regard, microtwin nucleation in Ni-based superalloys shares some similarities with twin formation in nanograined materials [48–52]. The γ/γ' interfaces in the superalloy work as partial dislocation sources analogous to grain boundaries in nanograined materials.

A microtwin embryo can form within the γ' phase by the glide of leading partial dislocations with identical Burgers vectors on consecutive upper or lower {111} planes. In competition, APB slip of γ' precipitates can occur when the leading partial dislocation is followed by a trailing partial dislocation on the same plane forming jointly a full type dislocation as indicated in Fig. 14a. Following the approach of McCabe et al. [48], the total force $F_{partial}$ per unit length L exerted on either the trailing partial or twin partial follows

$$\frac{F_{partial}}{L} = \frac{-F_{rep} + F_{fault} + F_\tau}{L} \tag{10}$$

where F_{rep} is the elastic repulsion due to the leading partial dislocation, F_{fault} is the contribution resulting from the change in fault energy due to the trailing partial and F_τ is the external force produced by the shear stress. Here, we have assumed that the complex extrinsic stacking fault (CESF-2) associated with the microtwin formation can be treated as two consecutives complex intrinsic faults (CISFs) over two adjacent {111} planes [53]. Therefore, the term $F_{fault}/L = \gamma_{CESF-2} - \gamma_{CISF} \approx \gamma_{CISF}$ for the case of the microtwin and $F_{fault}/L = \gamma_{APB} - \gamma_{CISF}$ for the case of APB shearing as indicated in Fig. 14b. The external force is equal to $F_\tau/L = b\,\sigma$ SF where σ is the uniaxial applied stress and SF is the Schmid factor of the dislocation. The elastic repulsion component has been proven to be the same for both configuration of partials [48].

Table 3
Parameters used for calculating the homogenised microtwin strain rates in MD2.

a(m)	b(m)	W(m)	L(m)	ϕ	$f_{\gamma'}$(%)
3.5×10^{-10}	1.4×10^{-10}	1.6×10^{-3}	1×10^{-3}	35.3°	63

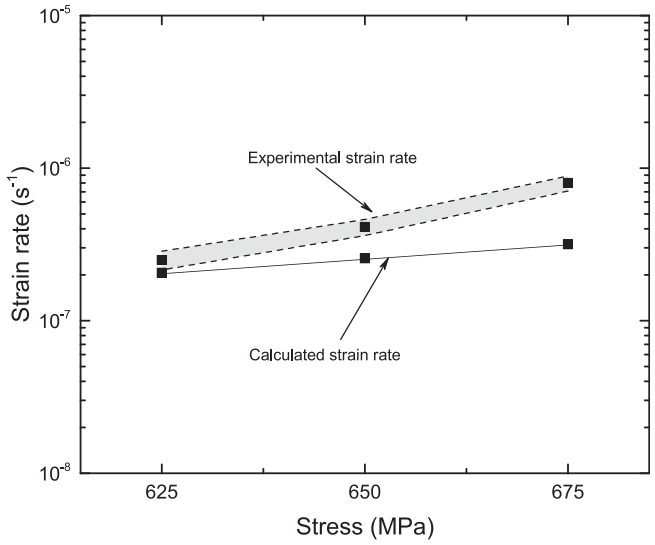


Fig. 13. Calculated and experimentally measured steady creep strain rates (with standard deviation) for MD2 single crystal superalloy at 800 °C and at 625 MPa, 650 MPa and 675 MPa.

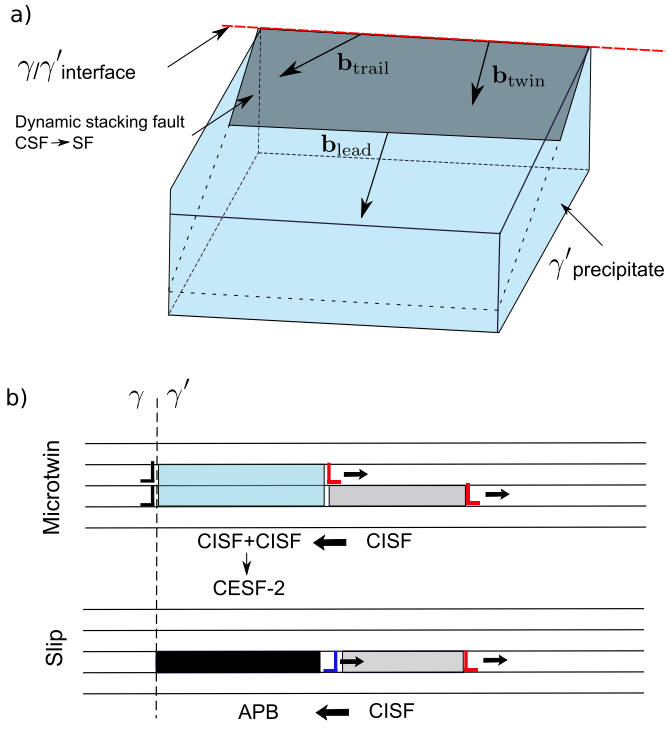


Fig. 14. Schematic diagram of the twin nucleation geometry for Ni-based superalloys. A leading partial dislocation is generated from the γ/γ' interface forming a faulted structure along the twin plane. At high temperatures, this fault structure is evolving as Cr and Co partition around the leading partial (CSF → SF). Two cases can occur: a new twin partial enters the precipitate on a consecutive gliding plane leading to a twin embryo, or the already dissociated trailing slip partial on the same plane enters the precipitate leading to an APB. Whether the driving force for twinning or slip is preferred depends on the time available for transforming to a low energy SF determined by the dislocation velocity. Adapted from McCabe et al. [48].

Microtwinning becomes favourable when the driving force for nucleation of a twinning partial is greater than the driving force for gliding of a trailing partial ($F_{\text{twin}} - F_{\text{trailing}} > 0$). This criterion leads to the following critical stress for microtwin nucleation

$$\sigma_{\text{cri}} > \frac{2\gamma_{\text{CISF}} - \gamma_{\text{APB}}}{b\left(\text{SF}_{\text{twin}} - \text{SF}_{\text{trailing}}\right)} \tag{11}$$

At the same time, the stress on the twin partial dislocation must be higher than the energy threshold for twin partial formation which can be approximated by: $\sigma_{\text{tw}} > \gamma_{\text{CISF}}/(b\,\text{SF}_{\text{twin}})$. The critical stress for microtwin nucleation satisfying both conditions is shown in Fig. 15 as a function of the crystal orientation. The tensile or compressive character of the required load is specified in Fig. 15a and the different stress levels are indicated in Fig. 15b for three different cases: first a completely unsegregated fault (CESF-2), second a partially partitioned fault with 50% of the original fault energy and finally the totally reordered case where the fault can be identified with a perfect SESF. Fault energies used are $\gamma_{\text{APB}} = 147\ \text{mJ/m}^2$, $\gamma_{\text{CISF}} = 177\ \text{mJ/m}^2$ and $\gamma_{\text{SESF}} = 74\text{mJ/m}^2$ [53]. The energy reduction promoted by the segregation and the atomic reordering of the fault leads to twin nucleation with stresses below 700 MPa, comparable with the experimental observations. The benefits of this approach are clear if polycrystalline aggregates are to be modelled in the future, leading to a criterion map of the stress for nucleation as a function of the stress state and the grain orientation. Further *ab initio* calculations of the influence of the partitioning phenomenon on the microtwin nucleation are required to obtain better estimates, but the tendency is clear: ⟨011⟩ and ⟨001⟩ crystal directions are the most prone orientations for creep twin formation followed by ⟨111⟩. This clearly coincides with the observations made in the literature which indicate that the ⟨011⟩ and ⟨001⟩ orientations are the most favourable for microtwinning [10,20,21,24].

A new variable is hereby added to the complexity of the microtwin formation: a time dependent nucleation mechanism. At this point, the main aspects of the formation of microtwins have been studied; however, some effects of microtwinning on the mechanical behaviour of the alloy are still unclear. This is the focus of the next section.

4.5. Implications of microtwinning

One of the most critical requirements for superalloys is the avoidance of brittle behaviour. Several authors have reported fatigue embrittlement in superalloys when microtwins appear during thermo-mechanical fatigue tests [54–58]. The link between microtwins and crack propagation is still controversial. In our study, a systematic change of the failure event type between twinned conditions and non-twinned conditions is observed, which correlates with the morphology of the fractured surface. A comparative analysis of the tensile creep fracture surfaces is shown in Fig. 16a for the case of twinned and twin-free conditions. The fracture mode in the twinned specimens is clearly cleavage-like on the whole fracture surface with small ductile features in localised regions. This is usually associated with a brittle mode of fracture [59]. The fracture facets are oriented along the same {111} plane of the predominant microtwin system. In contrast, the fracture surfaces of the twin-free samples show multiple facets and dimpled regions, typical of ductile failure in single crystals [59]. The fracture surface morphology does not change substantially with testing temperature and stress among the twinned specimens as can be observed in Fig. 16a. These results validate the proposition that crack nucleation and growth in MD2 at 800 °C is enhanced due to microtwin formation.

To explain the observed link between microtwins and the embrittlement of the material, the dislocation density distribution around creep twins has been studied in detail, see Fig. 16b–d. The

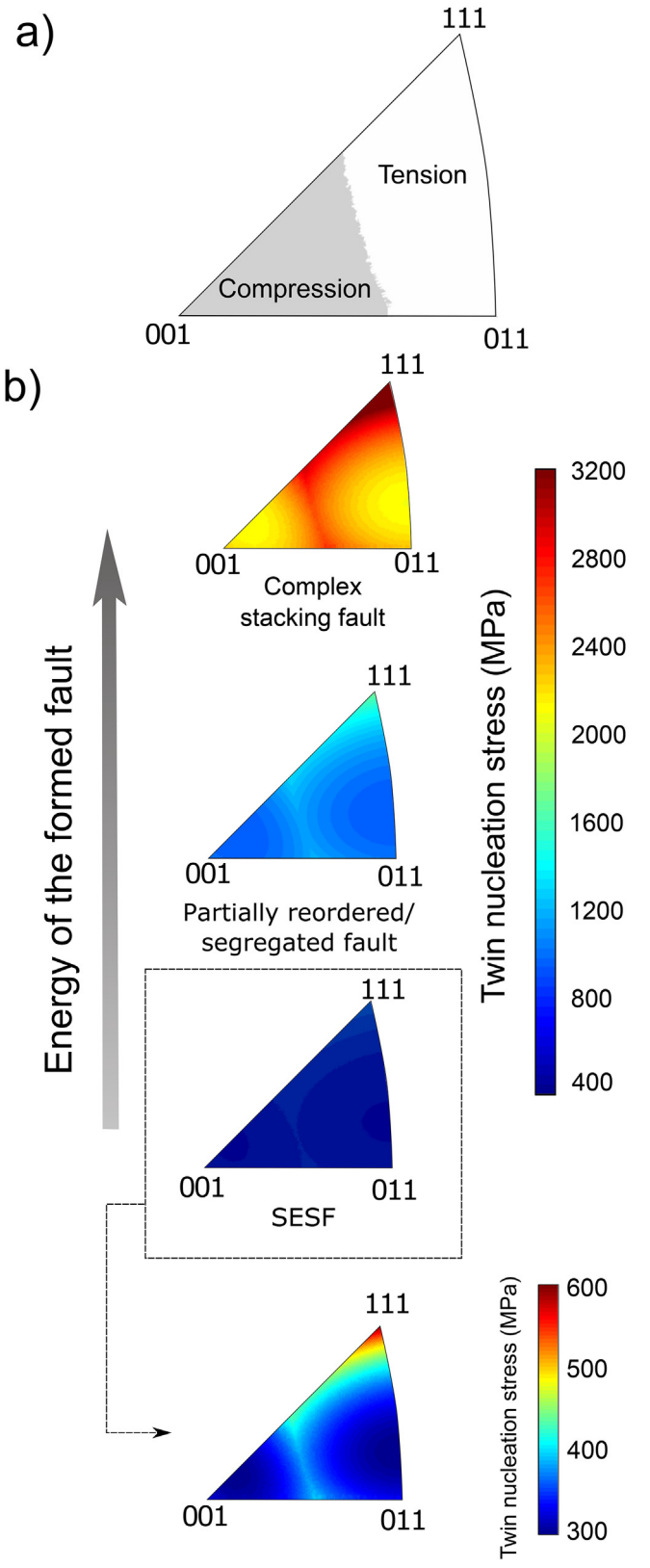


Fig. 15. Microtwin nucleation maps for a general Ni-based superalloy: a) tensile/compressive character of the twin stress; b) critical stress for microtwin nucleation for three cases of study: a completely unsegregated fault (top), a partially partitioned fault with 50% of the original fault energy (middle) and a totally reordered SESF fault (bottom), middle. Fault energies assumed are $\gamma_{APB} = 147\ mJ/m^2$, $\gamma_{CISF} = 177\ mJ/m^2$ and $\gamma_{SESF} = 74\ mJ/m^2$ [53].

spatially resolved geometrically necessary dislocation (GND) density has been calculated from high resolution (HR)-EBSD data and subsequent evaluation of Nye's dislocation tensor. The density distribution is shown in Fig. 16c. Higher dislocation density regions can be observed at the twin boundaries. This phenomenon is caused by dislocation pile-up events at the twin boundaries that can be explained by the abrupt change of Schmid factor at the twin-matrix interface $(0.47 \rightarrow -0.57)$ which locks the dislocation glide. These dislocations pile-ups can eventually cause stress concentrations which can lead to crack nucleation and propagation along the twin-parent interfaces as indicated in Fig. 16d. This mechanism causes brittle fracture when microtwins appear.

From this research, it follows that if the creep life of these materials is to be improved, consideration must be given to the factors influencing the appearance and thickening of microtwins. The results presented here indicate that the Co and Cr contents in the alloys might play an important role. This work lays the foundation for further studies on the influence of the alloy composition on diffusion-assisted fault formation (i.e., SESFs, SISFs or microtwins).

5. Summary and conclusions

Microtwinning in the single crystal superalloy MD2 has been studied. The following specific conclusions can be drawn:

1. For the single crystal superalloy MD2 tested along ⟨011⟩, microtwinning occurs for tensile stresses between 625 – 675 MPa and within the temperature interval 800 – 825 °C.
2. Microtwinning has been confirmed by using EBSD analysis. Twin fraction and twin thickness values have been measured by high resolution SEM analysis using electron channelling contrast. Higher stress causes a higher twinned fraction and thicker twins.
3. When microtwins are observed, their fraction and the assumed twinning shear can be used to estimate the twin strain produced, thus accounting for a significant part of the macroscopic creep strain observed experimentally (64–96% of the primary + secondary creep strain).
4. A new dislocation-based mechanism based on the decorrelation of partials is proposed for microtwin formation due to loading on the ⟨011⟩ direction; this is distinct from the ones in the literature for the more commonly studied ⟨001⟩ direction. The twin partial configuration proposed is consistent with the 60° crystallographic rotation found by EBSD analysis.
5. The kinetics of the microtwinning process have been modelled using phase transformation theory to account for the effects of temperature, stress and alloying. Physical constants (diffusion coefficients, concentrations of thermodynamic equilibrium and dislocation densities) are determined from thermodynamic databases, atom probe tomography, microstructural analysis and physical insights into the process.
6. The modelling allows for the recovery of the creep rate with reasonable accuracy. Temperature and stress dependences are also captured and compared with experimental results. At this scale, the acquired mechanistic knowledge of the microtwinning process allows for a better understanding of the deformation modes occurring in these materials.
7. A criterion for microtwin nucleation is introduced. Studying the influence of stress and temperature on the nucleation stress reveals the necessity for long range diffusion if microtwinning is to occur. This finding emphasises the crucial role that the alloy composition plays on microtwin nucleation kinetics.
8. The microtwinning mechanism alters the fracture mechanism and thus causes a degree of embrittlement. This observation may be of some practical importance.

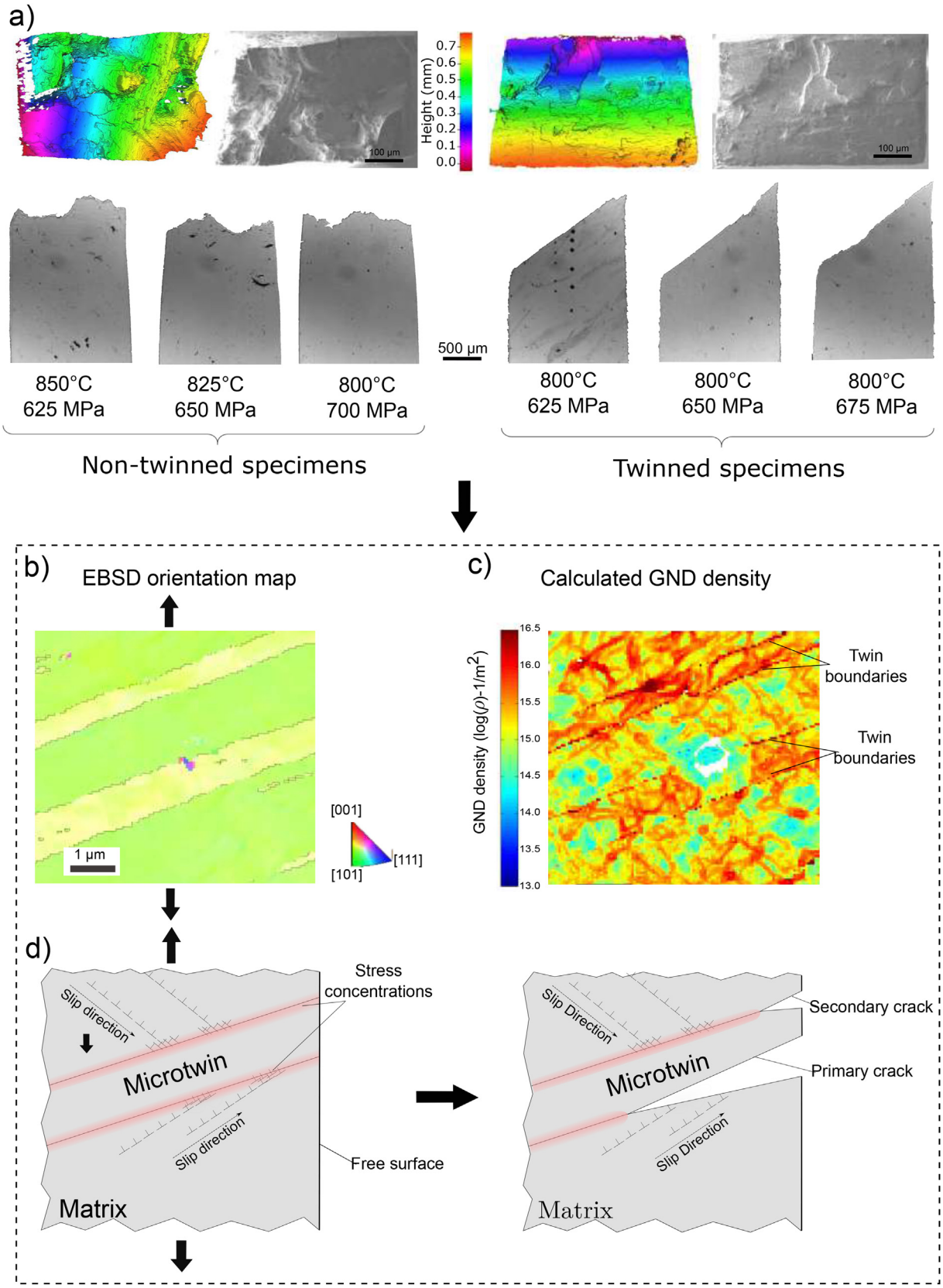


Fig. 16. a) Scanning electron micrographs and fracture surface topography analysis are illustrated for the specific cases of non-twinned sample tested at 850 °C-625 MPa (top-left) and twinned sample at 825 °C-625 MPa (top-right). Images of the fracture sections of twinned and non-twinned samples for several conditions showing the change of fracture mechanism (bottom); b) EBSD map of the twinned region after creep testing at 800 °C and 650 MPa (yellow bands represent microtwins); c) HR-EBSD dislocation density map from the same area; d) micromechanical model of the crack initiation and propagation at the twin boundaries. (For interpretation of the references to colour in this figure legend, the reader is referred to the web version of this article.)

Acknowledgements

The authors of this paper are grateful to J. Moverare and M. Segersäll of Linköping University for providing the studied material and for their assistance. The authors also thank P. Kontis and A. Németh for their assistance during the experimental campaign. Funding from the Engineering and Physical Sciences Research Council (EPSRC) of the UK is acknowledged under Grant EP/M50659X/1. The atom probe facility was funded by EPSRC grant EP/M022803/1.

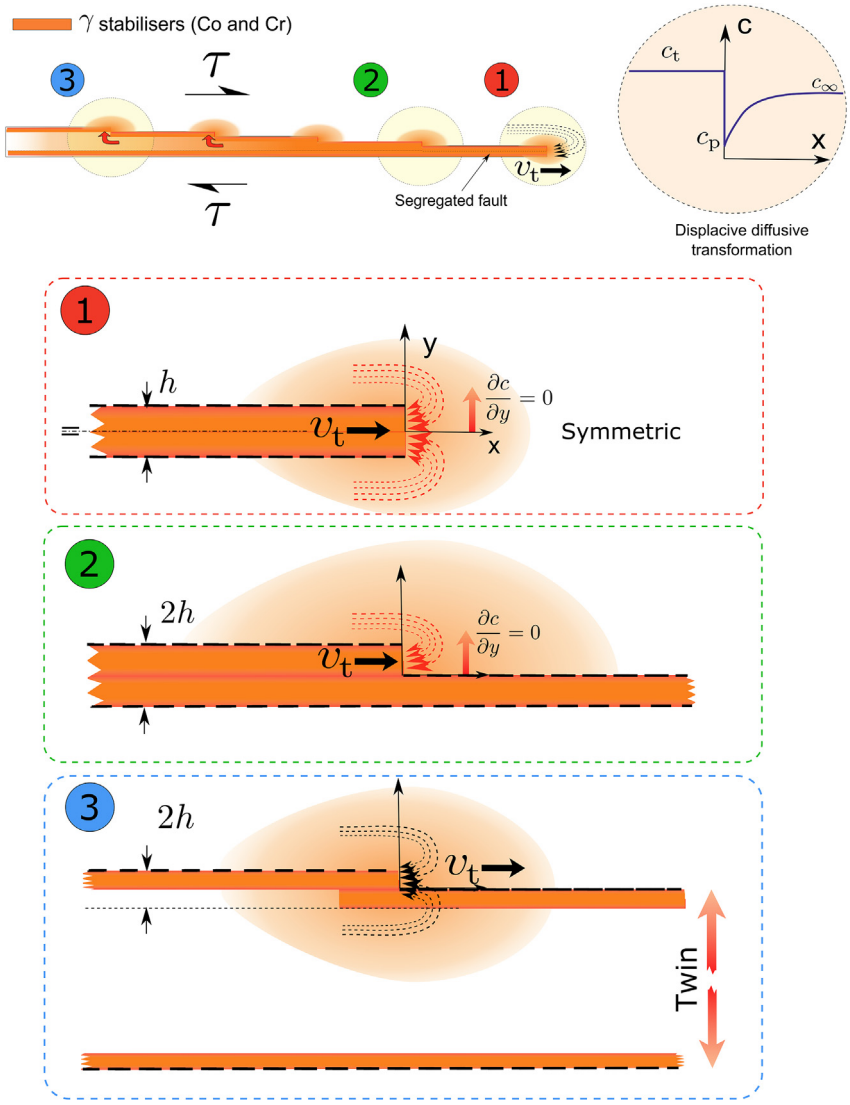


Fig. A1. Microtwin growing in the γ'-phase by a ledge-type mechanism (top). Three different diffusion problems can be identified along the twin: (1) growth of the twin tip in a virgin material with Co and Cr support exclusively from the surrounding material; (2) at the initial stage of growth, when the microtwin is still a few atomic planes thick and therefore the available Co an Cr to segregate small, the additional Co an Cr for thickening might need to still be supported by bulk diffusion from the matrix; (3) Once the twin thickens, the diffusion support of Co and Cr is not constrained anymore to the the matrix but also to the twin body.

Appendix A. Analysis of diffusion-assisted twin growth

In this section, a simple model for diffusion-assisted twinning is proposed. The elements Cr and Co are assumed to control twin lengthening and thickening. The important aspect is to consider carefully the length-scale associated with this.

There are at least three possible scenarios of importance, see Fig. A1. We identify first the situation at the very leading tip of the twin, labelled 1. Second, we consider the situation a little way back from the leading tip, just a few ledges away, labelled scenario 2; here it can be anticipated that the twin is still remarkably thin such that there is a need to support significant long-range bulk diffusion of Co/Cr from the surrounding matrix; this is because there is no substantial volume of twin to support a diffusional flux from it. Note that under these geometrical assumptions the ledge velocity is expected to be less than for scenario 1.

A third scenario relates to the situation far behind the leading tip when the twin is now much thicker. Here, in agreement with the experimental data, the bulk of the twin is no longer enriched with Cr/Co consistent with the need only for diffusion-controlled migration of the ledges. Therefore, the ledge migrates but with a diffusion field which is now – to a first approximation – symmetrical across the twin/matrix interface.

The above and, in particular, the velocity calculated is also

potentially modified by the fact that the ledge can grow along a terrace ahead of it which is enriched with respect to Cr/Co, compared to the mean composition of those elements in the alloy.

We now proceed to analyse the above scenarios with a particular emphasis on determining the ledge velocity in each case:

Scenario 1

Initially, the twin tip advances supported by bulk diffusion, broadly similar to a plate growth-like problem (see Fig. A1-scenario 1). For this case, the mathematical procedure developed by Atkinson [42] can be adapted assuming a no flux condition on the plane of symmetry $\left(\frac{\partial c}{\partial y}=0\right)$. Then, the problem is reduced to solving the concentration field in the upper half of the symmetry plane with a characteristic length of $l_{\text{char}}=h/2$. At the leading edge, the Stefan condition must be satisfied to accomplish mass conservation:

$$v_t = D_{\text{eff}}\frac{\partial c}{\partial X}\bigg|_{\text{step}}\left(c_t - c_p\right)^{-1} \tag{A1}$$

where the definition of the terms is given in the text. At this stage, the required support of solute for growth is exclusively bulk diffusion, so it seems reasonable to consider diffusion solely in the parent phase around the twin, governed by Fick's laws [60], whereas for simplicity, negligible diffusion occurs in the twin at this stage [42].

The diffusion problem is formulated in a moving non-dimensional coordinate system, $x=2(X-v_t)/h$ and $y=2\,Y/h$ (relative to stationary coordinates $X-Y$). Introducing the Péclet number $p=v_t h/4D$, one has:

$$\begin{cases} \nabla^2\Gamma(x,y)+2p\dfrac{\partial\Gamma}{\partial x}=0 \\ \dfrac{\partial\Gamma}{\partial y}=0 \text{ on } y=1, x<0 \\ \dfrac{\partial\Gamma}{\partial y}=0 \text{ on } y=0, x>0 \\ \dfrac{\partial\Gamma}{\partial x}=-\alpha^{-1}(p) \text{ on } x=0, 0\le y<1 \end{cases} \tag{A2}$$

where $\alpha(p)=-\left(\frac{\partial\Gamma}{\partial x}\Big|_{\text{step}}\right)^{-1}$ is an unknown function to be determined (assumed constant here as a first approximation) and the dimensionless concentration is defined by

$$\Gamma(x,y)=\frac{c(x,y)-c_\infty}{c_e-c_\infty} \tag{A3}$$

Two cases are studied for the interface boundary condition: first, we assume that the equilibrium concentration is achieved at the interface ($c_p=c_e$). Second, we include the effect of the interface reactions (short range reordering) on the twin kinetics by considering deviations from the equilibrium at the interface ($c_p\neq c_e$). For this case, the extra-boundary condition needed is imposed by accounting for the mobility μ_0, which is controlled by short-range atomic reshuffling:

$$v_t=\mu_0\left(c_p-c_e\right) \tag{A4}$$

In case of large μ_0 the problem is diffusion-controlled ($\mu_0\to\infty$ implies $c_p\to c_e$), whereas for small μ_0 the problem is reaction-controlled. A non-dimensional interface mobility is introduced in the problem: $q=\mu_0(c_t-c_e)(4D/h)^{-1}$.

The approximated solution using Fourier transforms and perturbation theory proposed by Atkinson [42] leads to a set of two non-linear equations for $0.003\le p<0.500$

$$\begin{cases} \alpha(p)=\pi^{-1}\{1-C+\ln(2\pi/p)\} \\ \Omega_0=2p\alpha(p)+(p/q)\{1-2p\alpha(p)\} \end{cases} \tag{A5}$$

where $C=0.5772\ldots$ is the Euler constant. In this system, $\alpha(p)$ and p are the unknowns to be determined and Ω_0 is defined as the dimensionless normalised supersaturation concentration $\Omega_0=(c_\infty-c_e)/(c_t-c_e)$. Once this system is solved, the velocity of the twin ledge can be recovered from the definition of Péclet number consistent with

$$v_t=\frac{4pD}{h} \tag{A6}$$

and the concentration field far from the twin tip can be approximated by the zero order Bessel function K_0 following Ref. [42]:

$$c(x,y)=\frac{\alpha}{p}K_0\{pr\}\exp\{-px\} \tag{A7}$$

where $r=\sqrt{x^2+y^2}$.

This process allows for the estimation of v_t as a function of the geometry h, assuming D and the concentration values. The diffusion field around the leading twin tip is presented in Fig. 11, being the diffusion scale roughly an order of magnitude larger than the twin height. The dependence of the leading twin tip velocity on the concentration ratio between the twin and the matrix is plotted as a function of the interface mobility in Fig. 12. It is noticeable that this problem is analogous to the diffusion-assisted shearing of other faults [23,24] and therefore the study could be extended to APBS, SISFs or SESFs.

Scenario 2

In this case, it is assumed that the microtwin is growing on a preformed twin. For the avoidance of doubt, in this case the assumption made is that the main diffusion flux is still limited to the surrounding matrix based on the argument that the reservoir of Co/Cr of the embryonic twin is still not enough to support the necessary partitioning of these elements to the new ledge. As is apparent, this problem shares the same mathematical structure as the one detailed in scenario 1 with the only difference being that the characteristic length in this case is $l_{\text{char}}=h$. Therefore the velocity resulting from the analysis is half the one considered in the previous case. The non-dimensional quantities and Péclet number remain the same as in scenario 1.

Scenario 3

Now, the growing front is advancing in a region where the concentration differs from the nominal concentration of the matrix due to the already enriched terrace ahead of it. Once the twin thickens, the partitioned region is now confined to the twin interfaces, leaving a region inside the twin with the same nominal concentration as the matrix. This problem resembles the one proposed in scenario 1, with a different concentration assumed ahead of the growing ledge (c_∞). But if it is assumed that the homogenised concentration ahead of the growing ledge (matrix + twin) is still close enough to the nominal matrix concentration ($\text{volume}_{\text{segregated}}\ll\text{volume}_{\text{non segregated}}$) the Péclet number for this scenario would be close to the one calculated for scenario 1. Therefore the velocity arising should be of the same order of

magnitude $\left(v_{case3} \approx v_{case1} \approx \frac{2D}{h}\right)$.

The characteristic lengths and approximate velocities of the three different scenarios are summarised in Table 4. The analysis presented here shows that, regardless of the growing stage of the twin (scenarios 1, 2 or 3), the growth velocity of the dislocation front is approximately $v_t \approx \frac{D}{h}$. Therefore, it seems reasonable to assume this estimation as a first approximation of the twin ledge velocity in Sec. 4.3.

Table 4
Velocities and characteristic lengths for the three different scenarios formulated in Appendix A.

	Scenario 1 (One Layer Fault)	Scenario 2 (Thin Twin)	Scenario 3 (Mature Twin)
Velocity	$\approx \frac{2D}{h}$	$\approx \frac{D}{h}$	$\approx \frac{2D}{h}$
Characteristic length	$\frac{h}{2}$	h	$\frac{h}{2}$

References

[1] C.D. Allen, Plasticity of Nickel-based Single Crystal Superalloy, Ph.D. thesis, Massachusetts Institute of Technology, 1995.
[2] R.C. Reed, The Superalloys: Fundamentals and Applications, 2006. Cambridge.
[3] M. McLean, G.A. Webster, F.R.N. Nabarro, A. Cottrell, Nickel-Base superalloys: current status and potential, Philos. Trans. Phys. Sci. Eng. 351 (1995) 419–433.
[4] R.N. Ghosh, R.V. Curtis, M. McLean, Creep deformation of single crystal superalloys — modelling the crystallographic anisotropy, Acta Metall. Mater. 38 (1990) 1977–1992.
[5] T.M. Pollock, A.S. Argon, Creep resistance of CMSX-3 nickel base superalloy single crystals, Acta Metall. Mater. 40 (1992) 1–30.
[6] E.I. Galindo-Nava, L.D. Connor, C.M.F. Rae, On the prediction of the yield stress of unimodal and multimodal γ' Nickel-base superalloys, Acta Mater. 98 (2015) 377–390.
[7] D.J. Crudden, A. Mottura, N. Warnken, B. Raeisinia, R.C. Reed, Modelling of the influence of alloy composition on flow stress in high-strength nickel-based superalloys, Acta Mater. 75 (2014) 356–370.
[8] Y.M. Eggeler, J. Mller, M.S. Titus, A. Suzuki, T.M. Pollock, E. Spiecker, Planar defect formation in the γ' phase during high temperature creep in single crystal coni-base superalloys, Acta Mater. 113 (2016) 335–349.
[9] G.B. Viswanathan, P.M. Sarosi, M.F. Henry, D.D. Whitis, W.W. Milligan, M.J. Mills, Investigation of creep deformation mechanisms at intermediate temperatures in René 88 DT, Acta Mater. 53 (2005) 3041–3057.
[10] L. Kovarik, R. Unocic, J. Li, P. Sarosi, C. Shen, Y. Wang, M.J. Mills, Microtwinning and other shearing mechanisms at intermediate temperatures in Ni-based superalloys, Prog. Mater. Sci. 54 (2009) 839–873.
[11] V.A. Vorontsov, R.E. Voskoboinikov, C.M.F. Rae, Prediction of mechanical behaviour in Ni-Base superalloys using the phase field model of dislocations, Adv. Mater. Res. 278 (2011) 150–155.
[12] V.A. Vorontsov, L. Kovarik, M.J. Mills, C.M.F. Rae, High-resolution electron microscopy of dislocation ribbons in a CMSX-4 superalloy single crystal, Acta Mater. 60 (2012) 4866–4878.
[13] R.R. Unocic, L. Kovarik, C. Shen, P.M. Sarosi, Y. Wang, J. Li, S. Ghosh, M.J. Mills, Deformation mechanisms in Ni-base disk superalloys at higher temperatures, in: R.C. Reed, K.A. Green, P. Caron, T. Gabb, M.G. Fahrmann, E.S. Huron, S.A. Woodard (Eds.), Superalloys 2008, the Minerals, Metals and Materials Society, 2008, pp. 377–385.
[14] P.M. Sarosi, G.B. Viswanathan, M.J. Mills, Direct observation of an extended complex stacking fault in the γ' phase of a Ni-base superalloy, Scr. Mater. 55 (2006) 727–730.
[15] M. Kolbe, The high temperature decrease of the critical resolved shear stress in nickel-base superalloys, Prog. Mater. Sci. A319–321 (2001) 383–387.
[16] M. Legros, N. Clement, P. Caron, A. Coujou, In-situ observation of deformation micromechanisms in a rafted γ/γ' superalloy at 850° C, Mater. Sci. Eng. A 337 (2002) 160–169.
[17] D.M. Knowles, S. Gunturi, The role of ⟨112⟩ {111} slip in the asymmetric nature of creep of single crystal superalloy CMSX-4, Mater. Sci. Eng. A 328 (2002) 223–237.
[18] B. Kear, J. Oblak, Deformation modes γ' precipitation hardened Ni-base superalloy, J. Phys. Colloq. 35 (1974) 35–45.
[19] D.M. Knowles, Q.Z. Chen, Superlattice stacking faul formation and twinning during creep in γ/γ' single crystal superalloy CMSX-4, Mater. Sci. Eng. A 340 (2003) 88–102.
[20] D. Barba, S. Pedrazzini, A. Vilalta-Clemente, A.J. Wilkinson, M.P. Moody, P.A.J. Bagot, A. Jérusalem, R.C. Reed, On the composition of microtwins in a single crystal nickel-based superalloy, Scr. Mater. 127 (2017) 37–40.
[21] T.M. Smith, R.R. Unocic, H. Deutchman, M.J. Mills, Creep deformation mechanism mapping in nickel base disk superalloys, Mater. High. Temp. 33 (2016) 1–12.
[22] L.P. Freund, O.M.D.M. Messé, J.S. Barnard, M. Göken, S. Neumeier, C.M.F. Rae, Segregation assisted microtwinning during creep of a polycrystalline L12-hardened Co-base superalloy, Acta Mater. 123 (2017) 295–304.
[23] M.S. Titus, A. Mottura, G.B. Viswanathan, A. Suzuki, M.J. Mills, T.M. Pollock, High resolution energy dispersive spectroscopy mapping of planar defects in $L1_2$-containing Co-base superalloys, Acta Mater. 89 (2015) 423–437.
[24] T.M. Smith, B.D. Esser, N. Antolin, G.B. Viswanathan, T. Hanlon, A. Wessman, D. Mourer, W. Windl, D.W. McComb, M.J. Mills, Segregation and η phase formation along stacking faults during creep at intermediate temperatures in a Ni-based superalloy, Acta Mater. 100 (2015) 19–31.
[25] T.M. Smith, B.D. Esser, N. Antolin, A. Carlsson, R.E.A. Williams, A. Wessman, T. Hanlon, H.L. Fraser, W. Windl, D.W. McComb, M.J. Mills, Phase transformation strengthening of high-temperature superalloys, Nat. Commun. 7 (2016) 13434.
[26] J.W. Christian, S. Mahajan, Deformation twinning, Prog. Mater. Sci. 39 (1995) 1–157.
[27] S. Karthikeyan, R.R. Unocic, P.M. Sarosi, G.B. Viswanathan, D.D. Whitis, M.J. Mills, Modeling microtwinning during creep in Ni-based superalloys, Scr. Mater. 54 (2006) 1157–1162.
[28] N. Zhou, C. Shen, M.J. Mills, J. Li, Y. Wang, Modeling displacive-diffusional coupled dislocation shearing of γ' precipitates in Ni-base superalloys, Acta Mater. 59 (2011) 3484–3497.
[29] H.K.D.H. Bhadeshia, Diffusional and displacive transformations, Scr. Metall. 21 (1987) 1017–1022.
[30] G.B. Olson, H.K.D.H. Bhadeshia, M. Cohen, Coupled diffusional/displacive transformations, Acta Metall. 37 (1989) 381–390.
[31] G.J. Jones, R.K. Trivedi, Lateral growth in solid-solid phase transformations, J. Appl. Phys. 42 (1971) 4299–4304.
[32] Y. Li, G. Purdy, On the growth of Widmanstatten precipitates in an Al-Cu alloy, Acta Mater. 56 (2008) 364–368.
[33] Y.M. Zhu, A.J. Morton, J.F. Nie, Growth and transformation mechanisms of 18R and 14H in Mg–Y–Zn alloys, Acta Mater. 60 (2012) 6562–6572.
[34] S.A. Mujahid, H.K.D.H. Bhadeshia, Coupled diffusional/displacive transformations: effect of carbon concentration, Acta Metall. Mater. 41 (1993) 967–973.
[35] B. Roebuck, D.C. Cox, R.C. Reed, An innovative device for the mechanical testing of miniature specimens of superalloys, in: K.A. Green, H. Harada, T.E. Howson, T.M. Pollock, R.C. Reed, J.J. Schirra, S. Walston (Eds.), Superalloys 2004, the Minerals, Metals and Materials Society, 2004, pp. 523–528.
[36] A.J. Wilkinson, G. Meaden, D.J. Dingley, High-resolution elastic strain measurement from electron backscatter diffraction patterns: new levels of sensitivity, Ultramicroscopy 106 (2006) 307–313.
[37] A.J. Wilkinson, E.E. Clarke, T.B. Britton, P. Littlewood, P.S. Karamched, High-resolution electron backscatter diffraction: an emerging tool for studying local deformation, J. Strain Anal. Eng. Des. 45 (2010) 365–376.
[38] J. Svoboda, P. Lukis, Activation energy of creep in <001>-orientated superalloy CMSX-4 single crystals, Mater. Sci. Eng. A 234–236 (1997) 173–176.
[39] G.L. Drew, R.C. Reed, K. Kakehi, C.M.F. Rae, Single crystal superalloys: the transition from primary to secondary creep, in: K.A. Green, H. Harada, T.E. Howson, T.M. Pollock, R.C. Reed, J.J. Schirra, S. Walston (Eds.), Superalloys 2004, the Minerals, Metals and Materials Society, 2004, pp. 127–136.
[40] C.N. Reid, W.S. Owen, Deformation Geometry for Materials Scientists, Pergamon Press, Oxford, 1973.
[41] G.B. Viswanathan, R. Shi, A. Genc, V.A. Vorontsov, L. Kovarik, C.M.F. Rae, M.J. Mills, Segregation at stacking faults within the γ' phase of two Ni-base superalloys following intermediate temperature creep, Scr. Mater. 94 (2014) 5–8.
[42] C. Atkinson, The growth kinetics of individual ledges during solid/solid phase transformations, in: Proceedings of the Royal Society of London, 1981, pp. 351–368.
[43] G. Schoeck, The activation energy of dislocation movement, Phys. Status Solidi (b) 8 (1965) 499–507.
[44] J.P. Hirth, W.D. Nix, An analysis of the thermodynamics of dislocation glide, Phys. Status Solidi (b) 35 (1969) 177–188.
[45] J.O. Andersson, T. Helander, L. Höglund, P. Shi, B. Sundman, Thermo-Calc & DICTRA, computational tools for materials science, Calphad 26 (2002) 273–312.
[46] TTNI8, -Thermotech Ni-based superalloys database v8.0, Accessed January 2015.
[47] F. Pyczak, B. Devrient, H. Mughrabi, The effects of different alloying elements on the thermal expansion coefficients, lattice constants and misfit of nickel-based superalloys investigated by X-Ray diffraction, in: K.A. Green, H. Harada, T.E. Howson, T.M. Pollock, R.C. Reed, J.J. Schirra, S. Walston (Eds.), Superalloys 2004, the Minerals, Metals and Materials Society, 2004, pp. 827–836.
[48] R.J. McCabe, I.J. Beyerlein, J.S. Carpenter, N.A. Mara, The critical role of grain orientation and applied stress in nanoscale twinning, Nat. Commun. 5 (2014) 3806.
[49] A. Jérusalem, M. Dao, S. Suresh, R. Radovitzky, Three-dimensional model of strength and ductility of polycrystalline copper containing nanoscale twins, Acta Mater. 56 (2008) 4647–4657.
[50] Y.T. Zhu, X.Z. Liao, S.G. Srinivasan, E.J. Lavernia, Nucleation of deformation twins in nanocrystalline face-centered-cubic metals processed by severe

plastic deformation, J. Appl. Phys. 98 (2005) 1–8.
[51] F. Wu, Y.T. Zhu, J. Narayan, Macroscopic twinning strain in nanocrystalline Cu, Mater. Res. Lett. 2 (2014) 63–69.
[52] L. Li, C. Ortiz, Pervasive nanoscale deformation twinning as a catalyst for efficient energy dissipation in a bioceramic armour, Nat. Mater. 13 (2014) 501–507.
[53] V.A. Vorontsov, R.E. Voskoboinikov, C.M.F. Rae, Shearing of γ' precipitates in Ni-base superalloys: a phase field study incorporating the effective γ-surface, Philos. Mag. 92 (2012) 608–634.
[54] H.U. Hong, B.G. Choi, I.S. Kim, Y.S. Yoo, C.Y. Jo, Deformation behavior during thermo-mechanical fatigue of a nickel-based single crystal superalloy, Procedia Eng. 10 (2011) 281–286.
[55] J. Kanesund, J.J. Moverare, S. Johansson, Deformation and damage mechanisms in IN792 during thermomechanical fatigue, Mater. Sci. Eng. A 528 (2011) 4658–4668.
[56] X.Z. Lv, J.X. Zhang, H. Harada, Twin-dislocation and twin-twin interactions during cyclic deformation of a nickel-base single crystal TMS-82 superalloy, Int. J. Fatigue 66 (2014) 246–251.
[57] F. Sun, J. Zhang, H. Harada, Deformation twinning and twinning-related fracture in nickel-base single-crystal superalloys during thermomechanical fatigue cycling, Acta Mater. 67 (2014) 45–57.
[58] J.J. Moverare, S. Johansson, R.C. Reed, Deformation and damage mechanisms during thermal-mechanical fatigue of a single-crystal superalloy, Acta Mater. 57 (2009) 2266–2276.
[59] A. Pineau, A.A. Benzerga, T. Pardoen, Failure of metals I: brittle and ductile fracture, Acta Mater. 107 (2016) 424–483.
[60] A. Fick, On liquid diffusion, Lond. Edinb. Dublin Philos. Mag. J. Sci. 10 (1855) 30–39.
[61] M.G. Ardakani, M. McLean, B.A. Shollock, Twin formation during creep in single crystals of nickel-based superalloys, Acta Mater. 47 (1999) 2593–2602.
[62] R.R. Unocic, G.B. Viswanathan, P.M. Sarosi, S. Karthikeyan, J. Li, M.J. Mills, Mechanisms of creep deformation in polycrystalline Ni-base disk superalloys, in: R.C. Reed, K.A. Green, P. Caron, T. Gabb, M.G. Fahrmann, E.S. Huron, S.A. Woodard (Eds.), Superalloys 2008, the Minerals, Metals and Materials Society, 2008, pp. 25–32.
[63] R.R. Unocic, N. Zhou, L. Kovarik, C. Shen, Y. Wang, M.J. Mills, Dislocation decorrelation and relationship to deformation microtwins during creep of a γ' precipitate strengthened Ni-based superalloy, Acta Mater. 59 (2011) 7325–7339.
[64] C. Tian, G. Han, C. Cui, X. Sun, Effects of stacking fault energy on the creep behaviors of Ni-base superalloy, Mater. Des. 64 (2014) 316–323.